PCCP

Accepted Manuscript

ROYAL SOCIETY OF CHEMISTRY

www.rsc.org/pccp

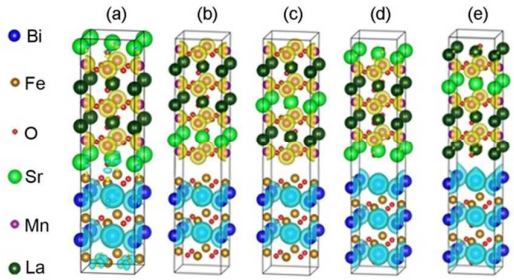

The magnetoelectric coupling can be realized in the tetragonal $La_{2/3}Sr_{1/3}MnO_3/BiFeO_3$ heterostructure by means of exchange bias.

First Principles Prediction of Interfacial Magnetoelectric Coupling in Tetragonal $La_{2/3}Sr_{1/3}MnO_3/BiFeO_3$ Multiferroic Superlattices

Nan Feng[1], Wenbo Mi[1,*], Xiaocha Wang[2,*]

[1]*Tianjin Key Laboratory of Low Dimensional Materials Physics and Preparation Technology, Faculty of Science, Tianjin University, Tianjin 300072, China*

[2]*Tianjin Key Laboratory of Film Electronic & Communicate Devices, School of Electronics Information Engineering, Tianjin University of Technology, Tianjin 300384, China*

[*]Author to whom all correspondence should be addressed.

E-mail: miwenbo@tju.edu.cn (W.B. Mi) and wangxccn@126.com (X.C. Wang)

ABSTRACT

The electronic structure and magnetic properties of the tetragonal $La_{2/3}Sr_{1/3}MnO_3/BiFeO_3$ multiferroic superlattices with different interfacial terminations have been studied by first-principles calculations. Our results for all the models of the tetragonal $La_{2/3}Sr_{1/3}MnO_3/BiFeO_3$ superlattices exhibit a metallic electronic structure. More importantly, we find that the magnetoelectric coupling can be realized in the tetragonal $La_{2/3}Sr_{1/3}MnO_3/BiFeO_3$ heterostructures by means of exchange bias, which can be attributed to the interfacial exchange coupling. These findings are useful for the magnetoelectric controlled spintronic devices.

Keywords: Multiferroic; Magnetic Properties of Interfaces; Exchange Interactions

PACS: 75.80.+q, 75.70.Cn, 75.30.Et

I. INTRODUCTION

The electric-field control of magnetization has motivated significant effort on the multiferroic materials.[1,2] $BiFeO_3$ (BFO) is a suitable multiferroic material for the magnetoelectric application because it has a direct coupling between the ferroelectric and antiferromagnetic order parameters at room temperature.[3] One of the most promising applications is the use of the antiferromagnetic BFO for the exchange bias in the antiferromagnetic/ferromagnetic heterostructures.[4] The electric controlled exchange bias has been demonstrated in a heterostructure composed of half-metallic $La_{2/3}Sr_{1/3}MnO_3$ (LSMO) and rhombohedral BFO (*R*-BFO), which may pave the way to the lower power devices with a smaller size.[5] So far, the LSMO/*R*-BFO bilayers has been a topic of much interest and debate.[6-8] X-ray magnetic circular dichroism measurements have demonstrated a significant exchange bias for the coupling between them mediated by an interfacial magnetic state,[9] and it is supposed to have different origins of the interfacial Fe ferromagnetic ordering like strong Mn-Fe hybridization,[9] Fe-O-Fe bond angle alteration and suppression of octahedral tiltings near the interface,[10] charge and orbital ordering,[11] and Fe/Mn intermixing,[12] The magnitude of induced Fe magnetization is proved to be sensitive to the size of band gap of BFO.[13]

Tetragonal BFO has a spontaneous polarization (150 $\mu C/cm^2$)[14], which is much higher than rhombohedral BFO (90 $\mu C/cm^2$).[15] Zhang *et al.* have provided the

experimental evidence for a large ferroelectric polarization in the tetragonal BFO and have attributed it to the pronounced strain-induced Fe displacements relative to the O octahedron.[16] Sun *et al.* have argued that a significantly enhanced exchange bias in the Fe_3O_4/tetragonal BFO bilayers comes from the stronger Fe-O-Fe interfacial superexchange in the distorted structure.[17] Actually, a bilayer with LSMO would definitely be an interesting system for the study of magnetoelectric coupling. In our previous work, the most energetically stable model in the tetragonal LSMO/BFO superlattices has exhibited a half-metallic characteristic and a stronger magnetoelectric effect by comparison with the *R*-BFO.[18] With the development of the film fabrications, the superlattices with the different terminations can be obtained even though they are energetically metastable. Therefore, in order to probe the possibility of the existence of exchange bias at the tetragonal LSMO/BFO interfaces so as to realize the magnetoelectric coupling, five possible candidate models with different terminations are considered. In this work, we present a theoretical study on the interfacial electronic structure and magnetic properties of the tetragonal LSMO/BFO multiferroic superlattices by density functional theory and analyze the origin of the interfacial Fe ferromagnetic ordering. These systems may have the promising to realize the exchange-bias coupling experimentally as observed in LSMO/*R*-BFO heterostructures[9] and have the potential applications in the magnetoelectric devices.

II. CALCULATION DETAILS AND MODELS

Our calculations are based on the density functional theory[19] with the generalized gradient approximation in the parameterization of Perdew-Burke-Ernzerhof[20] by using the plane-wave basis Vienna Ab initio Simulation Package code[21]. The pseudo potential is described by projector augmented wave method.[22] Additionally, all the calculations are performed by taking into account an on-site Coulomb interaction U for the localized d orbitals of the transitional metals. We set U=4.5 eV for Fe based on our previous electronic structure of bulk BFO, Fe_3O_4/$BiFeO_3$ superlattice[23] and Fe_4N/$BiFeO_3$ interface.[24] We have confirmed that the adopted U value is sufficient to describe the magnetic moment of Fe atoms, anti-ferromagnetic ordering, ferroelectricity, and the density of states of bulk $BiFeO_3$. U=2 eV is chosen for Mn, which reproduces the half-metallicity of LSMO, as reported in previous study.[25] Moreover, we set the plane-wave cutoff to 500 eV and employ the valence electron configurations: O $2s^2 2p^4$, Mn $3d^6 4s^1$, Fe $3d^7 4s^1$, Sr $4s^2 4p^6 5s^2$, La $5p^6 5d^1$, and Bi $6s^2 6p^3$. Γ-centered 9×9×9 and 9×9×1 k-meshes are used for the bulk compounds and superlattices, respectively. The convergence criterion is set as 10^{-5} eV in energy and 0.01 eV/Å in force.

Tetragonal BFO with a space group of $P4mm$ has a lattice constant of a=3.94 Å and c/a=1.02.[26] O_A and O_B belong to the BiO and FeO layers, respectively. The

magnetic order of G-type or C-type has not been clear in the tetragonal phase film.[27] Herewith, we consider the G-type antiferromagnetism, where the Fe atoms are ferromagnetically coupled within the (111) planes and antiferromagnetically coupled between the adjacent (111) planes.[28] Tetragonal LSMO with space group of *P*4*mm* has a lattice constant of a=3.88 Å and c/a= 3.00.[29] The unit cell contains 15 atoms in four layers: SrO, LaO, Mn_AO_2 and Mn_BO_2. The Mn_A atom sees a SrO layer below and a LaO layer on top, whereas Mn_B atom sees LaO layers on both sides. The superlattice is modeled by a slab geometry consisting of seven LSMO(001) atomic layers on the top of five BFO(001) atomic layers. And it is based on an $\sqrt{2}\times\sqrt{2}$ in-plane supercell in order to accommodate the BFO's G-type antiferromagnetic ordering. The calculated in-plane lattice mismatch between BFO(001) and LSMO(001) is 1.4%. This allows us to use the average lattice constant in the *ab*-plane of the supercells. To investigate the interfacial magnetic coupling, five LSMO/BFO superlattices with the different terminations have been employed, as shown in Fig. 1.

III. RESULTS AND DISCUSSION

The optimized structural parameters of the superlattices are listed in Table 1. The interlayer distances are different at two interfaces in each model, which indicates that the interfacial interactions are different. The shortest interlayer distance is 2.01 Å,

which occurs in model a where the interfacial O atoms sit directly on top of Fe atoms. No significant octahedral tilting and rotations, but Mn atoms shifts off the centers of O octahedral in the LSMO regions of the superlattices. Defining the atomic displacements of O relative to cationic plane in two interfacial regions, we find the O atoms either move towards or away from their adjacent interfaces. The O atoms of the Bi(Fe)-$O_A(O_B)$ planes in layer I are displaced away from the interface and those in layer V are displaced towards their adjacent interface, indicating that every O atom is displaced in the same direction. This fact indicates a resulting net polarization in BFO region pointing to layer V. Furthermore, BFO is subject to a reduced ferroelectric polarization, which is reflected by smaller Bi/Fe-O displacements than bulk (0.79/0.61 Å). The similar extent of geometry deformations of $Fe(O_B)_2$ on the MnO_2 terminations of LSMO (models b and c) indicates similar interaction strength. The relative Sr-O displacements in layer VII at the $Fe(O_B)_2$-terminated interfaces are inward 0.12 Å, which are the opposite sign with that between La/Sr and O atoms at the BiO_A-terminated interfaces. The Mn atoms in layers II and VI of model e lie farther from the interface than O atoms by a distance of 0.06 and 0.14 Å, respectively. The sign is the opposite as those in other models. These results indicate that O atoms may play an important role in mediating the interaction between BFO and LSMO. In this paper, we will concentrate on the comparison of electronic and magnetic properties of the two interfacial regions for each model and analysis the role of O atoms.

We start the analysis of the electronic structure in Figs. 2(a) and (b), which show the total and projected densities of states (DOS) of fully relaxed bulk BFO and LSMO, respectively. For BFO, the calculated band gap of 1.90 eV shows a good agreement with previous calculations,[23] but does not reach the experimental value of 2.50 eV[30] as a result of using the generalized gradient approximation. The contribution of Bi *s* states to bonding is negligible. The Fe spins are antiparallel but the DOS is the same, so that we only show one atom. The calculated Fe magnetic moment is ±4.18 μ_B/atom, which is identical to a previously reported value.[26] The LSMO DOS exhibits a half-metallic character with a spin-down band gap of 1.87 eV. The Mn_A and Mn_B magnetic moments are 3.42 and 3.68 μ_B, respectively, approaching the experimental value of 3.70 μ_B,[31] which confirms that the used parameters in the present work are reliable.

Fig. 3 illustrates the electronic band structures of models a, b and d. We find that the electronic properties of models b and c are analogous to each other, and model d has similar electronic properties to model e. The LSMO and BFO contributions to the eigenstates are shown by red and blue dots, respectively, where the size quantifies the contribution. The atomic termination is found to profoundly affect the properties of the heterostructure: in the $Fe(O_B)_2$-terminated interface, the half-metallic character of LSMO is lost in models b and c, whereas for the BiO_A-terminated interfaces the half-metallicity is preserved. For BFO side, the interaction with LSMO makes the semiconducting BFO transform into metallicity (models a, d, and e) or half-metallicity

(models b and c).

Table 2 reports the magnetic moments on the different atomic species near the interfacial layers of five models compared with bulk. As compared to bulk LSMO, the magnetic moments decrease by 7.24%, 5.60%, 6.99%, and 4.30% for models a, b, c, and d, respectively. However, it is slightly enhanced by 1.50% in model e. The resulting PDOSs for model a are shown in Fig. 4. The label "I-Fe(3)", for example, refer to "layer I" and "(3)" is the atomic number of Fe atom, as defined in Fig. 1. The same definition is used in other figures. For BFO, Fermi level (E_F) differs from bulk: in layer I it shifts towards a higher energy by 0.80 eV, while in layer V its energy is lowered by 0.90 eV into the valence band. Therefore, BFO shows a metallic character. A remarkable hybridization of Fe in layer I with O in layer I is seen in the energy range from –3.67 to 0.71 eV, suggesting the formation of covalent bonding. Although there is a strong hybridization between Fe in layer I and Mn_A in layer II via O in layer I in the energy range from –6.81 to –1.00 eV. However, the exchange coupling mediated by O atoms has almost no influence on the magnetic moments of Fe and Mn_A except for E_F shift. In contrast, the strong hybridization between Mn_A in layer VI and O in layer VII makes Mn_A hybridize with O_B in layer V in the energy range from –3.67 to 0.71 eV, which results in a decrease of Mn_A magnetic moment from 3.42 to 3.10 μ_B. This also leads to an induced O_B magnetic moment of 0.07 μ_B in layer V, which is antiparallel to Mn_A. The Mn_A-O_B hybridization strengthens the Fe-O_B hybridization, which lowers

the Fe magnetic moment. Especially, in the energy range from –3.47 to 0.52 eV, the hybridization of O_B with Fe(4) is stronger than Fe(5), making the Fe(4) magnetic moment reduce to 4.04 μ_B. This implies that an induced net Fe magnetic moment of 0.10 μ_B is antiparallel to Mn_A, as it has been demonstrated for LSMO/*R*-BFO bilayers.[9] In order to analyze the case of the spin polarization (*P*) at Fermi level for BFO, *P* is defined as $P=\left[N_{\uparrow}(E_F)-N_{\downarrow}(E_F)\right]/\left[N_{\uparrow}(E_F)+N_{\downarrow}(E_F)\right]$, in terms of the total DOS in the spin-up $N_{\uparrow}$ and spin-down channels $N_{\downarrow}$, respectively. The spin polarization can be derived from Fig. 4(a) as *P*=5.96% for model a.

By comparing the electronic structures of models b and c, one can find that the electronic states of BFO are similar, as shown in Figs. 5(a) and 6(a). The main difference is that E_F of LSMO region in model c relative to model b is slightly shifted towards lower energy. For model b, O *p* spin-down states in layer I go through E_F, destroying the half-metallicity of LSMO, whereas for model c, the absence of half-metallicity results from the contribution of O *p* and Mn *d* states in the spin-down channel in layers I and VII. In the following, we will concentrate mostly on model b, and only briefly mention the results for model c, as they have the same conclusions. As can be seen from Figs. 5(a) and 5(b), Fe in layer I and Mn_A in layer I are hybridized in the energy range from –5.87 to –0.83 eV so that the Fe spin-splitting decreases, resulting in a smaller Fe magnetic moment than bulk. The Mn_A-O hybridization in layers I is weaker than bulk, yielding an increased Mn_A magnetic moment. The O_B *p*

states in layer V hybridize with Mn_A *d* states in layer VII in the energy range from –1.64 to 1.32 eV. An alalogous behavior is also observed between Fe in layer V and Mn_A in layer VII, leading to the analogous to superexchange interaction between Fe and Mn_A mediated by O_B in layer V. The coupling makes electronic states of Fe atoms show a strong spin-splitting and produce spin-polarized carriers at E_F. This induced a net Fe magnetic moment of 0.85 μ_B is antiparallel to Mn_A. Importantly, the obtained Fe magnetic moment is similar to that observed previously by X-ray magnetic circular dichroism for LSMO/*R*-BFO bilayers (0.60 μ_B).[9] Therefore, our result also indicates the presence of interfacial coupling that can induce the exchange bias at the interface of LSMO/*T*-BFO, as that observed in LSMO/*R*-BFO.[9] This induces an O_B magnetic moment of 0.19 μ_B in layer V, which is parallel to Mn_A in layer VII. The exchange coupling makes the hybridization of Mn_A with O in layer VII weaker than bulk, which slightly increases Mn_A magnetic moment. Furthermore, a larger Mn_A magnetic moment in layer VII than that in layer I comes from a weaker hybridization with O on the same layers. In model c, a stronger Mn_B-O hybridization in layers I and VII result in decreased Mn_B magnetic moments. Meanwhile, by a stronger Mn_B-O hybridization in layer I than layer VII, the Mn_B magnetic moment is smaller. Furthermore, the hybridization between Mn in layer VII and O_B in layer V is stronger than model b in the energy range from –5.30 to 1.35 eV. We argue that exchange bias at the FeO_2-MnO_2 interfaces originated from the interfacial Fe-Mn exchange coupling

mediated by O_B can be the means to realize the magnetoelectric effect, with potential applications in spintronic devices.

The PDOSs of interfacial atoms in model d are qualitatively similar to model e [compare Figs. 7 and 8]. Therefore, in the following we will discuss model d in details and highlight the similarities and differences. For model d, we find that the electronic states of Bi in layer I show a strong spin-splitting at E_F, while those in layer V resemble bulk BFO. As shown in Figs. 7(a) and 7(b) that the hybridization of Bi in layer I with O in layer I through the interface around E_F and the hybridization of Mn_A in layer II with O in layer I in the energy range from –5.69 to 2.78 eV make the Bi-Mn_A hybridization appear in the energy range from –5.22 to 4.00 eV. The Bi-Mn_A hybridization makes the Bi magnetic moment be up to –0.38 μ_B. The magnetic moment is antiferromagnetically coupled to Mn_A via the intermediate O, leading to the conclusion that the analogous to the superexchange magnetic coupling path is Bi-O-Mn_A. This type of exchange coupling is not determined experimentally in the LSMO/*R*-BFO heterostructure but is concluded by the use of BFO in its tetragonal phase. The PDOSs of O_A atoms in layers I and V are relatively symmetrical, in accordance with the reduced O_A magnetic moments as compared to bulk. Interestingly, the electronic states go through E_F, destroying the original semiconducting characteristic. The electronic states of O_A in layer V become more localized. The Bi-O hybridization affects the corresponding O-Mn_A hybridization. The enhanced Mn_A-O

hybridization in layer II in the energy range from –7.24 to –1.10 eV leads to a smaller Mn_A magnetic moment than bulk. The electronic states of Mn_A and O in layer VI have a little difference from those in layer II. A remarkable hybridization of Mn_A in layer VI with O_A in layer V through O in layer VII is seen. Meanwhile, the enhanced Mn_A-O hybridization in layer VI in valence band slightly decreases the Mn_A magnetic moment as compared to bulk. For model e, because of a stronger Mn_B-O hybridization in layer II, Mn_B magnetic moment is smaller than bulk. A larger Mn_A magnetic moment in layer VI than bulk originates from weaker hybridization with O in layers VI and VII. The Bi-O hybridization in layer I around E_F is weaker than model d, so that the induced Bi magnetic moment is smaller. The hybridization between Mn_B in layer II and O in layer I is weaker than that between Mn_A in layer II and O in layer I in model d in the energy range from –3.00 to –0.94 eV, resulting in a larger Mn_B magnetic moment. A larger Mn_A magnetic moment in layer VI than model d can be attributed to weaker hybridization with O in layer VII. We find P=8.34% for model d and P=14.7% for model e deriving from Figs. 7(a) and 8(a), respectively. The total magnetic moments of BFO in models a-e are –0.37, –0.08, –0.04, –0.97, and –0.53 μ_B, respectively.

It is important to compare the strength of the magnetoelectric effect among five models. Due to the LSMO slab has a mirror plane in its central layer in FeO_2-SrO, FeO_2-Mn_BO_2, and BiO-SrO superlattices, the one interface is equivalent to another one with polarization reversal, the difference of the atomic magnetic moments at two

interfaces determines the magnetoelectric effect. For model a, we find a total magnetic moment of 6.77 μ_B for the interface (both labeled I in Fig. 1) and 5.82 μ_B for the interface (labeled VII and V in Fig. 1). The net magnetic moment change caused by the polarization reversal is about 0.95 μ_B for model a, which is similar to the value of 0.87 μ_B found in model d. This value is larger compared to that found in model c (0.02 μ_B), indicating stronger magnetoelectric coupling. The LSMO slab in models b and e does not fulfill the *c* direction 180º rotational symmetry, therefore, this method is not suitable to assess the magnetoelectric coupling strength. We find that, the total change in the magnetic moment at two interfaces with respect to bulk is 0.76 and 0.04 μ_B for models b and e, respectively. This suggests that, when an electric field is applied to the two configurations so as to reverse the ferroelectric polarization in BFO, the change of interfacial exchange coupling eventually will control LSMO magnetization. We note that model b has a stronger response to the variation of magnetic moment than model e, indicating a larger magnetoelectric effect.

The charge transfer at the interfaces is quantified by charge density difference calculations (see Fig. 1). The charge density difference $\Delta\rho$ is defined as $\Delta\rho = \rho - \rho_{slab}(\mathrm{LSMO}) - \rho_{slab}(\mathrm{BFO})$, where ρ, ρ_{slab}(LSMO), and ρ_{slab}(BFO) are charge densities of the superlattice, the LSMO, and the BFO slabs, respectively. As discussed above, the spontaneous polarization of BFO region points toward layer V. When LSMO is deposited on the top of BFO, the polar discontinuity at the interface leads to

divergence of the electrostatic potential when the number of BFO grows because of the periodic boundary conditions. To avoid the divergence, electrons in BFO can be transferred across the interface to LSMO region to form a build-in electric field pointing from BFO to LSMO. Therefore, we observe that charge accumulation appears in deeper Mn layers and charge depletion in deeper Bi layers. Especially, for model a, there is significant lost charge from O in layer I accumulating in the Fe-O bond region. This confirms that the formation of covalent bonding, in consistence with the above PDOS analysis. Furthermore, it is clear that the O_B in layer V lose charge, which is mainly redistributed around the O in layer VII and Mn in layer VI. For models d and e, we find that there is significant charge accumulation around O layer in layer I, VII. Our calculations indicate that the interfacial O atoms are responsible for the observed magnetoelectric coupling effect exhibited at the LSMO/BFO interface. All calculations above are based on the perfect interface. In practice, the situation may be complex, growth in an environment with low oxygen partial pressure could lead to the formation of oxygen vacancies in the interfacial region. Such oxygen treatment may influence the observed magnetoelectric coupling strength.

IV. CONCLUSION

In summary, we have investigated the electronic and magnetic properties of the

tetragonal LSMO/BFO(001) superlattices based on first principle calculations. It is found that all the five possible stacking models considered reveal that LSMO/BFO superlattices all exhibit metallic electronic properties. We have identified the presence of exchange bias at the tetragonal LSMO/BFO interface as a possible pathway to realize electric control magnetism, in agreement with the experimental findings in the heterostructure consisting of LSMO and rhombohedral BFO. The interfacial magnetoelectric effect is sensitive to the choice of the interfacial structure and originates from the interfacial exchange coupling. We hope that our theoretical prediction on the magnetoelectric coupling in tetragonal BFO/LSMO heterostructures can stimulate further experimental confirmation.

ACKNOWLEDGEMENTS

This work was supported by the NSFC of China (51171126), Key Project of TSTC of Tianjin (12JCZDJC27100 and 14JCZDJC37800), Program for NCET in University (NCET-13-0409) and Scientific Research Foundation for the Returned Overseas Chinese Scholars, State Education Ministry of China. It is also supported by High Performance Computing Center of Tianjin University, China.

REFERENCES

1 T. Kimura, T. Goto, H. Shintani, K. Ishizaka, T. Arima and Y. Tokura, *Nature*, 2003, **426**, 55.

2 W. Prellier, M. P. Singh and P. Murugavel, *J. Phys. Condens. Matter*, 2005, **17**, R803.

3 G. Catalan and J. F. Scott, *Adv. Mater.*, 2009, **21**, 2463.

4 K. D. Sung, T. K. Lee, Y. A. Park, N. Hur and J. H. Jung, *Appl. Phys. Lett.*, 2014, **104**, 252407.

5 S. M. Wu, S. A. Cybart, P. Yu, M. D. Rossell, J. X. Zhang, R. Ramesh and R. C. Dynes, *Adv. Mater.*, 2010, **9**, 756.

6 H. Béa, M. Bibes, M. Sirena, G. Herranz, K. Bouzehouane, E. Jacquet, S. Fusil, P. Paruch, M. Dawber, J.P. Contour and A. Barthélémy, *Appl. Phys. Lett.*, 2006, **88**, 062502.

7 J. Jilili, U. Eckern and U. Schwingenschlögl, *EPL*, 2013, **102**, 67009.

8 H. Y. Guo, J. G. Lin, J. C. Yang and Y. H. Chu, *Appl. Phys. Lett.*, 2014, **105**, 112406.

9 P. Yu, J. S. Lee, S. Okamoto, M. D. Rossell, M. Huijben, C. H. Yang, Q. He, J. X. Zhang, S. Y. Yang, M. J. Lee, Q. M. Ramasse, R. Erni, Y. H. Chu, D. A. Arena, C. C. Kao, L. W. Martin and R. Ramesh, *Phys. Rev. Lett.*, 2010, **105**, 027201.

10 A. Y. Borisevich, H. J. Chang, M. Huijben, M. P. Oxley, S. Okamoto, M. K. Niranjan, J. D. Burton, E. Y. Tsymbal, Y. H. Chu, P. Yu, R. Ramesh, S. V. Kalinin

and S. J. Pennycook, *Phys. Rev. Lett.*, 2010, **105**, 087204.

11 M. J. Calderón, S. Liang, R. Yu, J. Salafranca, S. Dong, S. Yunoki, L. Brey, A. Moreo and E. Dagotto, *Phys. Rev. B*, 2011, **84**, 024422.

12 R. F. Neumann, M. Bahiana and N. Binggeli, *EPL*, 2012, **100**, 67002.

13 S. Singh, J. T. Haraldsen, J. Xiong, E. M. Choi, P. Lu, D. Yi, X. D. Wen, J. Liu, H. Wang, Z. Bi, P. Yu, M. R. Fitzsimmons, J. L. MacManus-Driscoll, R. Ramesh, A. V. Balatsky, J. X. Zhu, and Q. X. Jia, *Phys. Rev. Lett.*, 2014, **113**, 047204.

14 A. J. Hatt and N. A. Spaldin, *Phys. Rev. B*, 2010, **81**, 054109.

15 Y. H. Chu, L. W. Martin, M. B. Holcomb and R. Ramesh, *Mater. Today*, 2007, **10**, 16.

16 J. X. Zhang, Q. He, M. Trassin, W. Luo, D. Yi, M. D. Rossell, P. Yu, L. You, C. H. Wang, C. Y. Kuo, J. T. Heron, Z. Hu, R. J. Zeches, H. J. Lin, A. Tanaka, C. T. Chen, L. H. Tjeng, Y. H. Chu and R. Ramesh, *Phys. Rev. Lett.*, 2011, **107**, 147602.

17 M. Y. Sun, P. Li, C. Jin, L. Y. Wang, D. X. Zheng and H. L. Bai, *EPL*, 2014, **105**, 17007.

18 N. Feng, W. B. Mi, X. C. Wang, Y. C. Cheng and U. Schwingenschlögl, Submitted.

19 W. Kohn and L. J. Sham, *Phys. Rev.*, 1965, **140**, A1133.

20 J. P. Perdew, K. Burke and M. Ernzerhof, *Phys. Rev. Lett.*, 1996, **77**, 3865.

21 G. Kresse and J. Furthmüller, *Phys. Rev. B*, 1996, **54**, 11169.

22 P. E. Blöchl, *Phys. Rev. B*, 1994, **50**, 17953.

23 H. Yang, C. Jin, W. B. Mi, H. L. Bai and G. F. Chen, *J. Appl. Phys.*, 2012, **112**, 063925.

24 N. Feng, W. B. Mi, X. C. Wang and H. L. Bai, *RSC Adv.*, 2014, **4**, 48848.

25 C. Wang, N. Stojić and N. Binggeli, *Appl. Phys. Lett.*, 2013, **102**, 152414.

26 H. M. Tütüncü and G. P. Srivastava, *Phys. Rev. B*, 2008, **78**, 235209.

27 D. Sando, A. Barthélémy and M. Bibes, *J. Phys.: Condens. Matter*, 2014, **26**, 473201.

28 D. H. Wang, W. C. Goh, M. Ning and C. K. Ong, *Appl. Phys. Lett.*, 2006, **88**, 212907.

29 F. Tsui, M. C. Smoak, T. K. Nath and C. B. Eom, *Appl. Phys. Lett.*, 2000, **76**, 2421.

30 R. Palai, R. S. Katiyar, H. Schmid, P. Tissot, S. J. Clark, J. Robertson, S. A. T. Redfern, G. Catalan and J. F. Scott, *Phys. Rev. B*, 2008, **77**, 014110.

31 J. L. Maurice, F. Pailloux, A. Barthélémy, O. Durand, D. imhoff, R. Lyonnet, A. Rocher and J. P. Contour, *Phil. Mag.*, 2003, **83**, 3201.

TABLE NOTES

Table 1 Average interlayer distance (Å) of BFO plane in layer I and LSMO plane in layer I (d) as well as interlayer distance between BFO plane in layer V and LSMO plane in layer VII (d'), and atomic displacements (Å) dz and dz' of interfacial O plane relative to cationic plane in the two interfacial regions for LSMO/BFO superlattices with five models, compare Fig. 1. Positive/negative numbers denote move towards/ away from their nearest interface.

	a	b	c	d	e
d	2.14	3.54	3.57	3.94	3.74
d'	2.01	3.75	3.79	3.91	3.69
$dz_{Bi/Fe}$	–0.20	–0.11	–0.11	–0.19	–0.34
dz_{Mn}	–0.10	–0.05	–0.13	–0.17	0.06
$dz_{La/Sr}$	0.12	—	—	0.08	0.22
$dz'_{Bi/Fe}$	0.23	0.16	0.16	0.50	0.59
dz'_{Mn}	–0.29	–0.27	–0.24	–0.17	0.14
$dz'_{La/Sr}$	–0.12	—	—	0.05	0.20

Table 2 The calculated magnetic moment $m(\mu_B)$ of Mn_A, Mn_B, O, Bi, O_A, Fe, and O_B for near interfacial layers as compared to bulk.

Atom	layer	Bulk	a	b	c	d	e
Mn_A	I	3.42	—	3.55	—	—	—
	II	3.42	3.41	—	—	3.35	—
	VI	3.42	3.10	—	—	3.33	3.48
	VII	3.42	—	3.73	—	—	—
Mn_B	I	3.68	—	—	3.59	—	—
	II	3.68	—	—	—	—	3.50
	VI	3.68	—	—	—	—	—
	VII	3.68	—	—	3.66	—	—
O	I	0.01	–0.07	0.05	–0.01	0	–0.02
	II	0.01	–0.01	—	—	0.02	0.02
	VI	0.01	–0.02	—	—	0.02	0.01
	VII	0.01	0.04	–0.02	–0.02	0.01	–0.03
Bi	I	0	—	—	—	–0.38	–0.15
	V	0	—	—	—	0	0
O_A	I	–0.21	—	—	—	–0.09	–0.11
	V	–0.21	—	—	—	0.05	0.01
Fe	I	±4.18	–4.18(3) 4.17(6)	–4.11(3) 4.12(6)	–4.10(3) 4.12(6)	—	—
	V	±4.18	–4.14(1) 4.04(4)	–4.17(1) 3.32(4)	–4.17(1) 3.31(4)	—	—
O_B	I	0	0	0	0	—	—
	V	0	–0.07	0.19	0.20	—	—

FIGURE CAPTIONS

FIG. 1. (Color online) Structure and charge density difference (isosurface value 0.01 e/Å^3) of the LSMO/BFO superlattice for (a) $Fe(O_B)_2$-SrO, (b) $Fe(O_B)_2$-Mn_AO_2, (c) $Fe(O_B)_2$-Mn_BO_2, (d) BiO_A-SrO, and (e) BiO_A-LaO. The yellow and blue isosurfaces ($\pm$0.01 e/Å^3) represent accumulation and depletion of electrons, respectively.

FIG. 2. (Color online) TDOS and PDOS of (a) BFO and (b) LSMO. The Fermi energy is indicated by vertical dashed lines and is set to zero.

FIG. 3. (Color online) Spin-up and spin-down band structures of the (a) model a, (b) model b, and (c) model d. The sizes of blue dots are proportional to the contributions from the BFO layers, whereas for red dots, the sizes are proportional to the contributions from the LSMO layers.

FIG. 4. (Color online) PDOS of interfacial BFO (a) and LSMO (b) in the fully relaxed LSMO/BFO superlattice for model a. The Fermi energy is indicated by vertical dashed lines and set to zero.

FIG. 5. (Color online) PDOS of interfacial BFO (a) and LSMO (b) in the fully relaxed LSMO/BFO superlattice for model b. The Fermi energy is indicated by vertical dashed lines and set to zero.

FIG. 6. (Color online) PDOS of interfacial BFO (a) and LSMO (b) in the fully relaxed LSMO/BFO superlattice for model c. The Fermi energy is indicated by vertical dashed lines and set to zero.

FIG. 7. PDOS of interfacial BFO (a) and LSMO (b) in the fully relaxed LSMO/BFO superlattice for model d. The Fermi energy is indicated by vertical dashed lines and set to zero.

FIG. 8. PDOS of interfacial BFO (a) and LSMO (b) in the fully relaxed LSMO/BFO superlattice for model e. The Fermi energy is indicated by vertical dashed lines and set to zero.

Fig. 1, N. Feng *et al*.

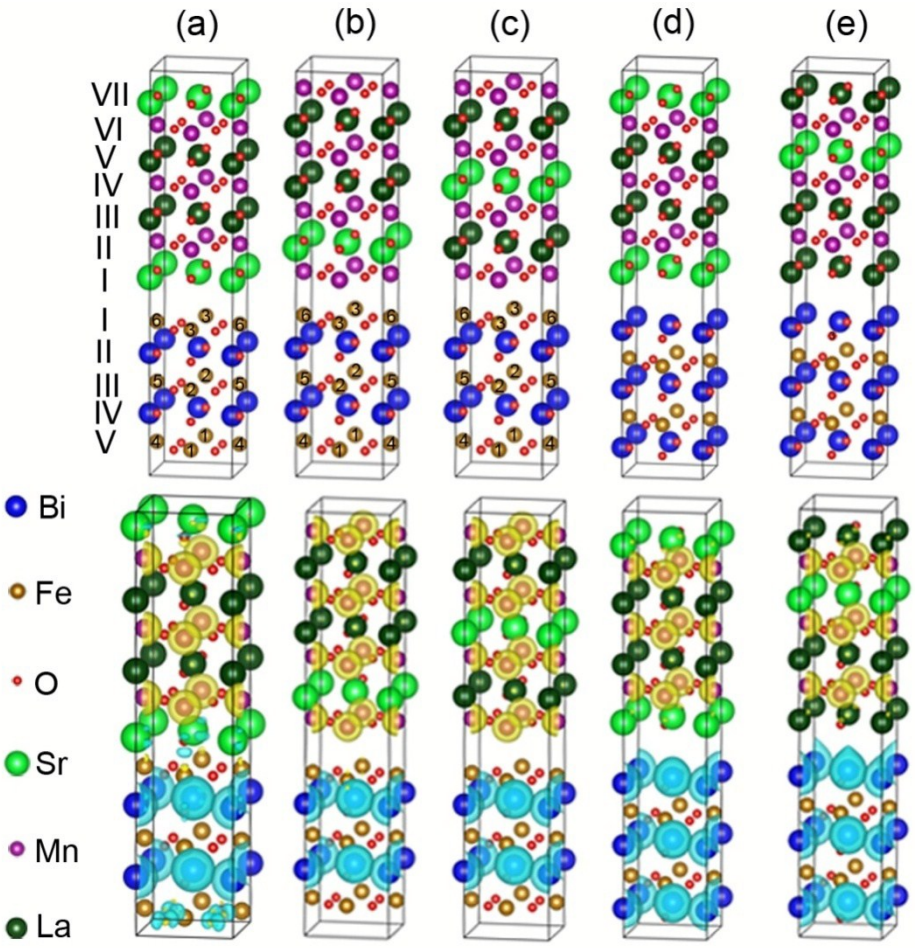

Fig. 2, N. Feng *et al*.

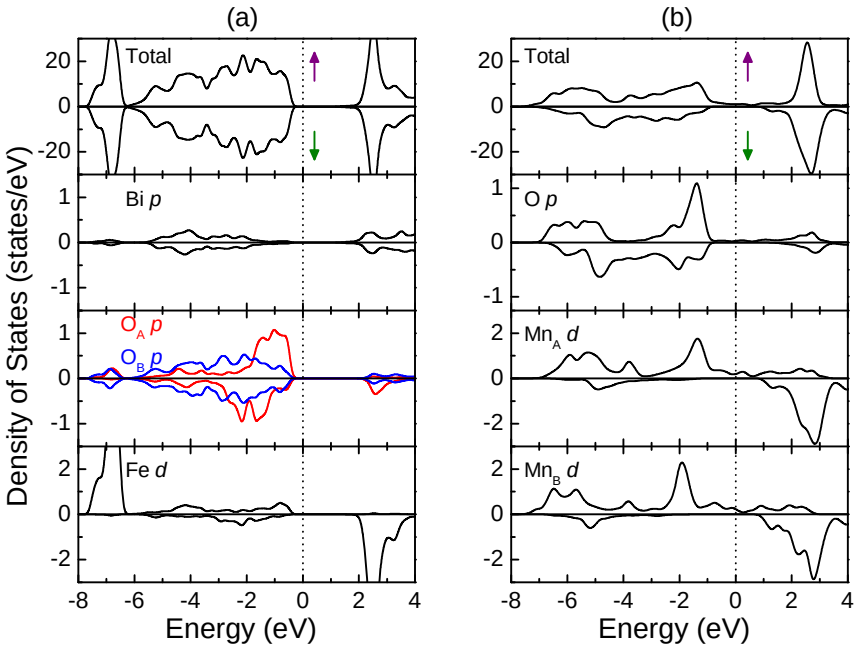

Fig. 3, N. Feng *et al*.

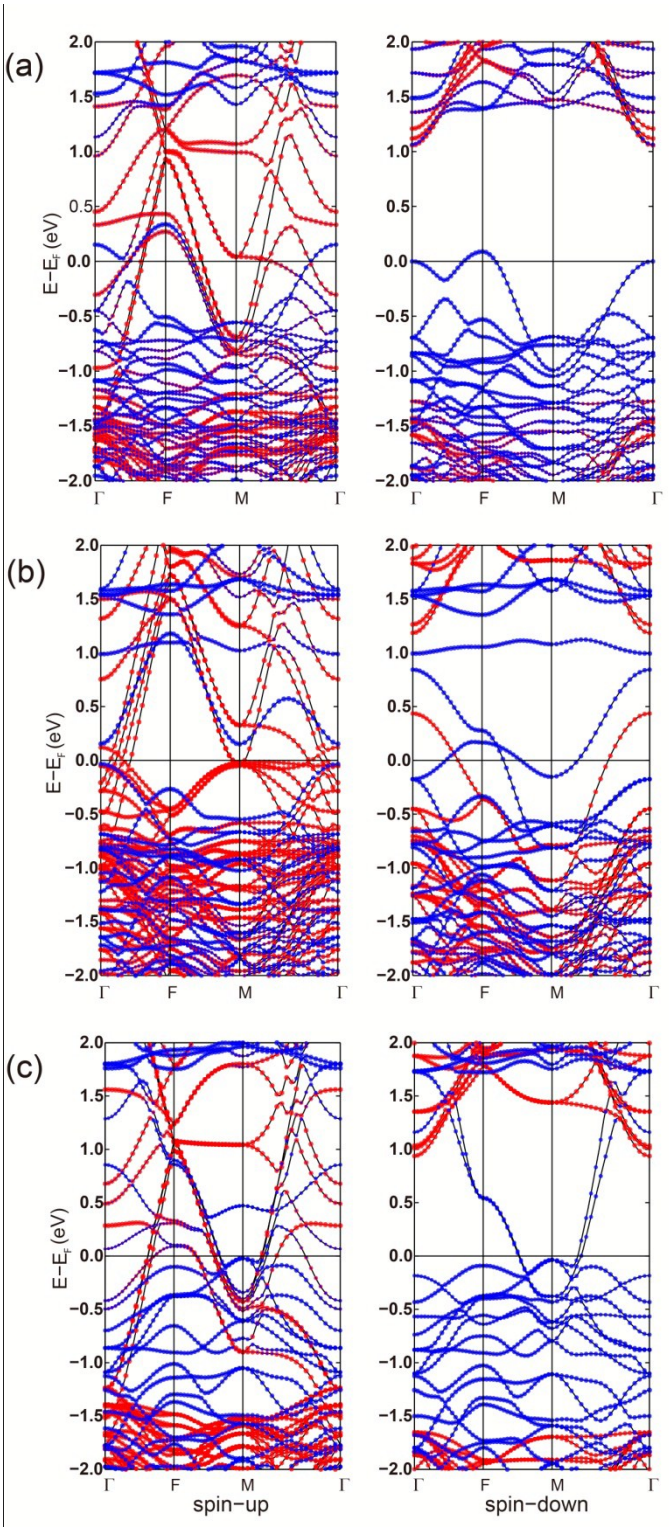

Fig. 4, N. Feng *et al*.

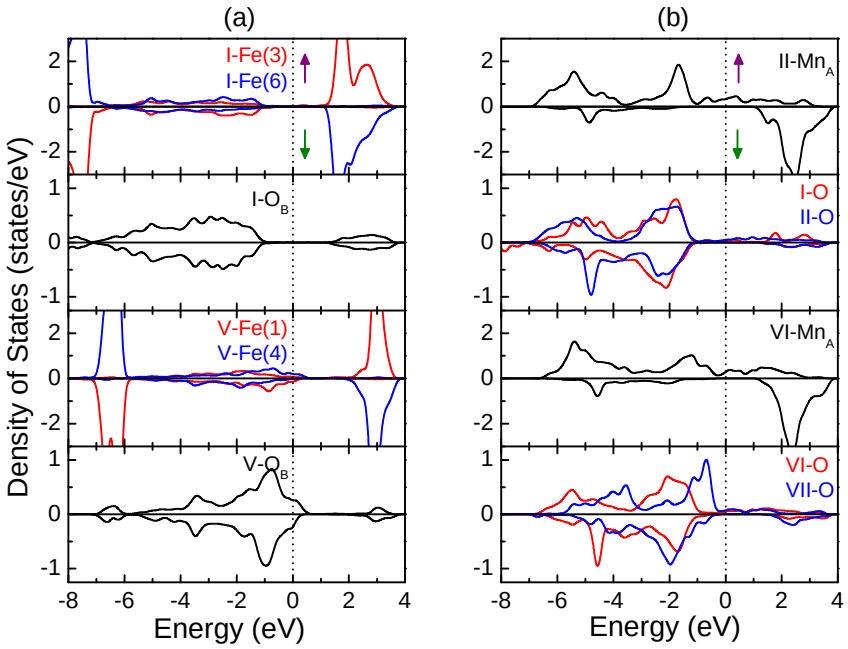

Fig. 5, N. Feng *et al*.

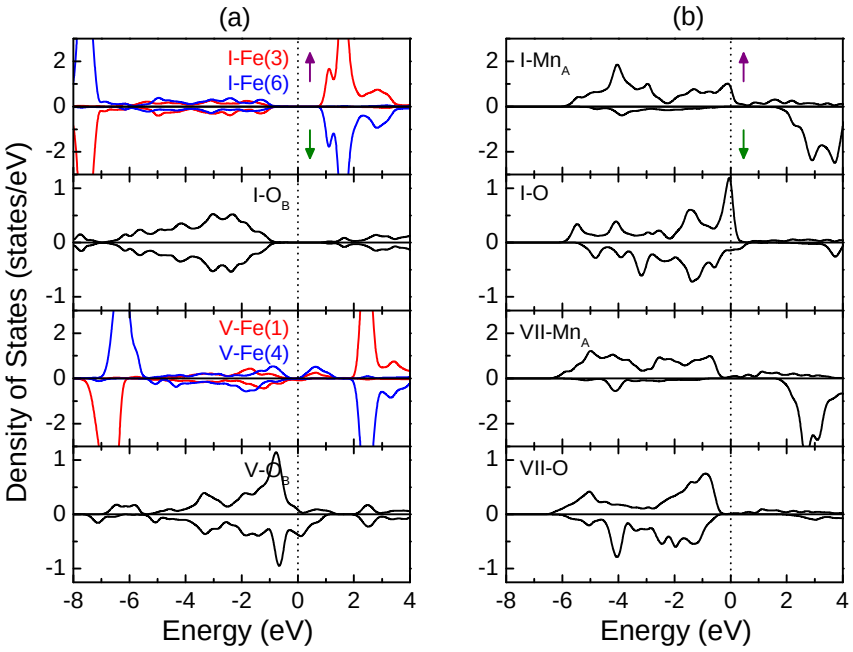

Fig. 6, N. Feng *et al*.

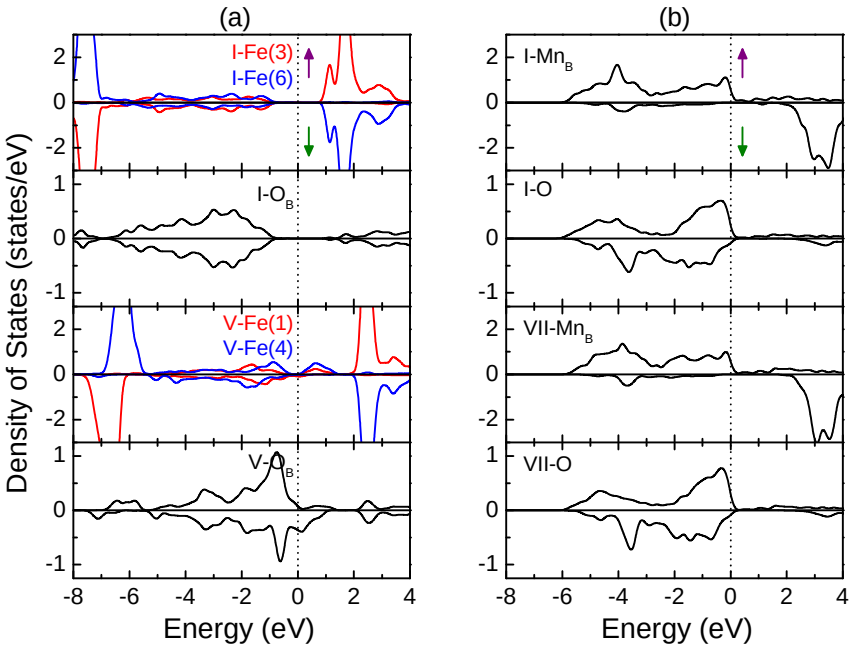

Fig. 7, N. Feng *et al*.

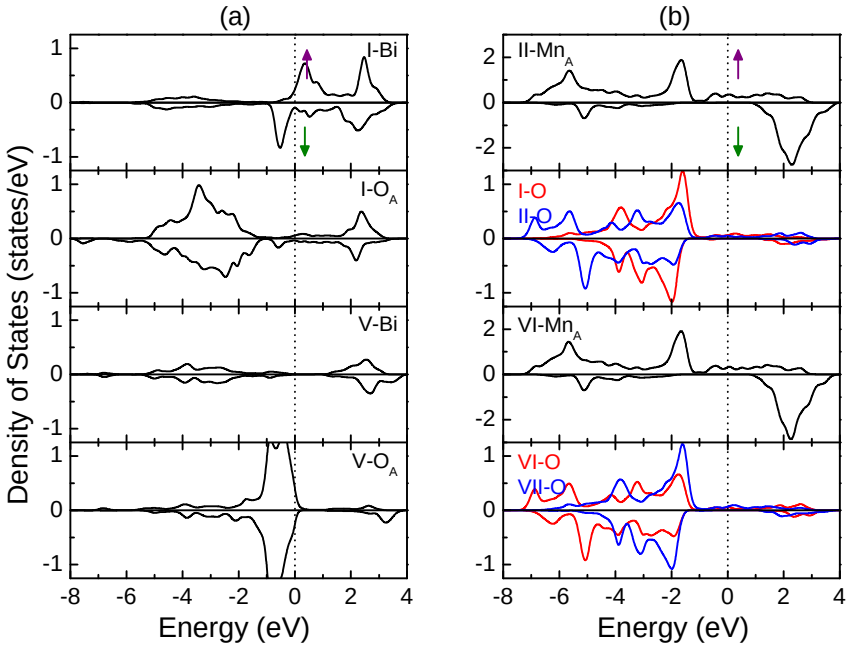

Fig. 8, N. Feng *et al*.